

# REDUCING VELOCITY ERROR AND ITS CONSEQUENCES BY AN ITERATIVE FEEDBACK IMMERSED BOUNDARY METHOD

Qiuxiang Huang<sup>1</sup>, Zhengliang Liu<sup>2</sup>, Abhijith Moni<sup>3</sup>, Sridhar Ravi<sup>1</sup>, Fang-Bao Tian<sup>1</sup>,  
John Young<sup>1</sup> and Joseph C. S. Lai<sup>1</sup>

<sup>1</sup> University of New South Wales  
ACT 2600, Australia  
qiuxiang.huang@adfa.edu.au

<sup>2</sup> Southern University of Science and Technology  
Shenzhen 518055, China  
liuzl3@sustech.edu.cn

<sup>3</sup> De Montfort University  
Leicester LE1 9BH, United Kingdom  
abhimon.kk@gmail.com

**Key words:** Immersed boundary method, Boundary velocity error, Streamline penetration, Blood flow

**Abstract.** The immersed boundary method (IBM) has attracted growing interest in the computational fluid dynamics (CFD) research community due to its simplicity in dealing with moving boundaries in fluid-structure interaction (FSI) systems. We present a study on streamline penetration, velocity error and consequences of a FSI solver based on an iterative feedback IBM. In the FSI, the fluid flows are solved by the lattice Boltzmann method; the solid structure deformation is solved by the finite difference method, and an iterative feedback IBM is used to realize the interaction between fluid and structure. The iteration can improve the no-slip and no-penetration boundary conditions at the fluid-solid interface. Four benchmark cases are simulated to study the reduced velocity error and its consequences: a uniform flow over a flapping foil, flow-induced vibration of a flexible plate attached behind a stationary cylinder in a channel, flow through a two-dimensional asymmetric stenosis and a one-sided collapsible channel. Results show that the iterative IBM can suppress the boundary-slip error and spurious flow penetration on the solid wall. While the iterative IBM does not have significant effect on the force production and structure deformation for external flows, it significantly improves the prediction of the force distribution and structure deformation for internal flows. The increased computational cost incurred by the iteration can be largely reduced by increasing the feedback coefficient. This study will provide a better understanding of the feedback IBM and a better option for the CFD community.

## 1 INTRODUCTION

The immersed boundary method (IBM) has attracted growing interest in the computational fluid dynamics (CFD) research community due to its simplicity in dealing with fluid-structure interaction (FSI) systems involving complex geometries and large deformations [1]. To improve the computational efficiency, the IBM was combined with the lattice Boltzmann method (LBM) by Feng and Michaelides [2] to simulate fluid-particles interactions. The immersed boundary-lattice Boltzmann method (IB-LBM) has since been implemented in many applications, including blood flow [3, 4, 5, 6], flapping wings [7]

and fish swimming [8].

Although the feedback IBM (including the direct-forcing version) has the advantage of simplicity, its accuracy and streamline penetration have been widely discussed [9, 10, 11]. However, the consequences of the boundary velocity error and the spurious flow penetration have not been discussed, especially for internal flows. In this study, we test the iterative effects of the IBM on streamlines and force distributions for external and internal flows.

## 2 NUMERICAL METHODS

In this study, the D2Q9 lattice Boltzmann method (LBM) with the multi-relaxation-time (MRT) model is adopted for the fluid dynamics. For FSI cases (e.g. flow-induced vibration of a flexible plate attached behind a stationary cylinder in a channel and a one-sided collapsible channel), the nonlinear dynamics of the structure is treated as a Bernoulli-Euler beam and solved by the finite difference method (FDM). The two-way fluid-structure interaction is implemented by the iterative feedback IBM. The details of these methods can be found in our previous publications [4, 12].

## 3 RESULTS

### 3.1 A uniform flow over a flapping foil

Here the simulation of a two-dimensional (2-D) NACA0012 foil in a uniform flow is conducted to test the iterative effect of the IB-LBM solver. The foil is pivoted at a point located on the chord line at  $0.5c$  from the leading edge, where  $c$  is the chord length. The pitching and heaving motions of the foil are described as

$$\theta(t) = \theta_0 \cos(2\pi ft), \quad (1)$$

$$h(t) = h_0 \cos(2\pi ft + \phi), \quad (2)$$

where  $\theta_0 = 10^\circ$  is the pitching amplitude,  $h$  is the vertical displacement,  $h_0 = 0.5c$  is the heaving amplitude, and  $\phi = 90^\circ$  is the phase angle between the two motions. The non-dimensional flapping frequency  $fc/U_0 = 0.5$ . The Reynolds number  $Re = U_0c/\nu = 1000$ , where  $U_0$  is the free-stream velocity. The computational domain is  $40c \times 30c$  with the minimum grid size of  $0.00625c$ . The non-dimensional drag  $C_D$  and lift  $C_L$  coefficients are defined to describe the aerodynamic forces on the foil,

$$C_D = \frac{F_D}{0.5\rho U_0^2 c}, \quad C_L = \frac{F_L}{0.5\rho U_0^2 c}, \quad (3)$$

where  $F_D$  and  $F_L$  are the drag and lift forces, respectively. Figure 1 shows the time histories of the drag  $CD$  and lift  $CL$  coefficients, which agree well with the computational result of Johnson & Tezduyar [13]. For the drag and lift coefficient computed by present three iteration strategies, the difference is negligibly small, indicating that iterations do not significantly improve the prediction of the force coefficients.

### 3.2 Flexible beam behind a stationary cylinder in a channel

Here, a moving boundary case, the FSI of a flexible plate behind a stationary cylinder in a channel, is considered. Figure 2 shows the schematic diagram of the geometry and the boundary conditions of this case. This case has been used as a benchmark validation for FSI solvers involving large-displacement. As shown in figure 2, a fixed circular rigid body is submerged in an incompressible fluid. A flexible

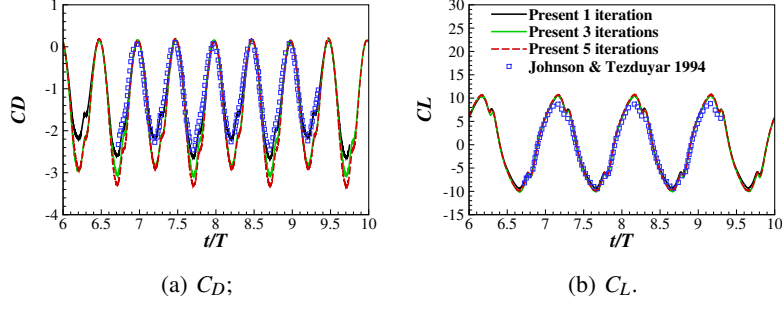


**Figure 1:** Comparison of drag and lift coefficients time histories for a NACA0012 flapping foil at  $Re = 1000$ .

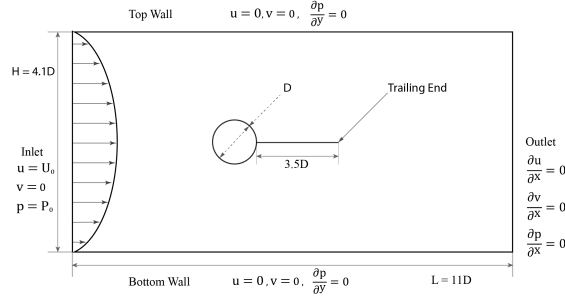


**Figure 2:** Schematic diagram of flow-induced vibration of a flexible beam behind a stationary cylinder.

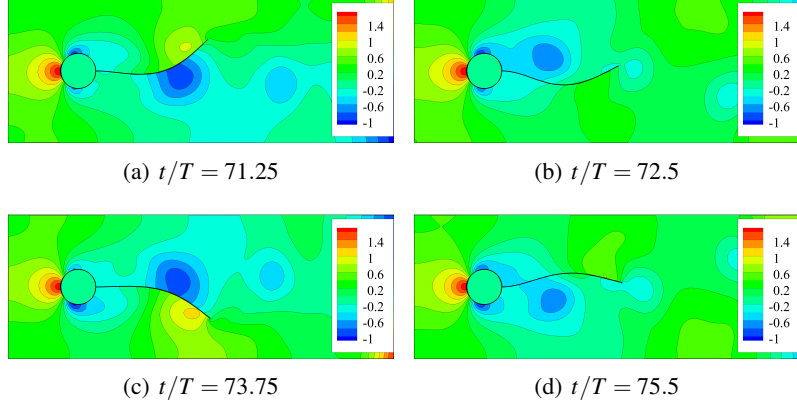
thin beam is attached downstream to the cylinder. The cylinder has a diameter of  $D$  and is centred at the origin. The beam has thickness  $h$  and length  $L = 3.5D$ . A parabolic velocity profile with averaged velocity  $U_0$  and a constant pressure  $P_0$  are imposed at the inlet. No-slip walls are enforced at the top and bottom sides of the computational domain. The normal and shear stress are set to zero at the outlet. The computational domain is a rectangular box ( $x \in [-2D, 9D]$  and  $y \in [-2.05D, 2.05D]$ ), and the grid size for the fluid and the beam is  $0.01D$  and  $0.005D$ , respectively. The non-dimensional parameters for this case are

$$Re = \frac{\rho U_0 L}{\mu}, \quad M = \frac{\rho_s}{\rho L}, \quad K_b = \frac{EI}{\rho U_0^2 L^3}, \quad K_s = \frac{Eh}{\rho U_0^2 L}, \quad (4)$$

where  $\rho_s$  is the linear density of the beam,  $M$  is the structure-to-fluid mass ratio, and  $K_b$  and  $K_s$  are the bending stiffness and stretching stiffness of the beam, respectively.  $E$  is Young's modulus, and  $I = h^3/12$  is the moment of inertia of the beam cross-section. Here  $Re = 100$ ,  $M = 2.0$ , and  $K_b = 1.111$ . A large stretching stiffness  $K_s = 500$  is chosen to achieve a nearly inextensible beam. Table 1 shows the comparison of the mean drag coefficient  $C_{D,m} = F_{D,m} / (0.5\rho U_0^2 D)$  ( $F_{D,m}$  is the mean drag of the cylinder-beam system), Strouhal number defined as  $St = fD/U_0$  ( $f$  is the oscillation frequency), and vertical oscillation amplitude of the trailing end. Overall, the present results show reasonable agreement with Tian et al. [14]. The Strouhal number  $St$ , which characterizes the flapping shedding frequency, is 0.186 in the present simulation with 1 iteration, while that computed by Tian et al. [14] is 0.19 (a difference of about 2.1%). In present simulation with 5 iterations,  $St = 0.181$  (a difference with Tian et al. [14] of 4.7%), suggesting iterations do not improve the prediction of the flapping frequency of the beam. Figure 3 displays pressure contours of the dynamic behaviour of the beam taken at four different

**Table 1:** Comparison of the mean drag  $C_{D,m}$ , Strouhal number  $St$ , and vertical oscillation amplitude  $A_m$  of the beam.

Sources	$C_{D,m}$	$St$	$A_m$
Tian et al. [14]	4.11	0.19	0.78
Present 1 iteration	3.70	0.186	0.87
Present 5 iterations	3.67	0.181	0.90


**Figure 3:** Pressure contours for flexible plate behind a stationary cylinder in a channel at different time instants. The pressure here is a relative pressure to the inlet pressure  $P_0$  and is non-dimensionalized by  $\rho U_0^2$ .

instants ( $t/T = 71.25; 72.5; 73.5; 75.5$ ) within an oscillation cycle. These results are in qualitative agreement with previous studies.

### 3.3 Fluid flow through a 2-D asymmetric stenosis

The iteration effects of the IBM are tested here for fluid flow through an asymmetric stenosis with a diameter restriction of 50% at the constriction. A cosine function dependent on the axial coordinate  $x$  is used to describe the upper stenosed channel wall,

$$y(x) = D \left[ 1 - a_0 \left( 1 + \cos\left(\frac{2\pi(x-x_0)}{L}\right) \right) \right], \quad (5)$$

where  $D$  is the diameter of the non-stenosed channel,  $a_0 = 0.25$  for the 50% diameter reduction,  $x_0 = 6$  is the  $x$  coordinate of the center of the stenosis ( $x_0 - L/2 \leq x \leq x_0 + L/2$ ), and  $L = 2D$  is the length of the stenosis. The length and width of the whole computational domain are  $16D$  and  $1.2D$ , respectively. A steady Poiseuille flow with an averaged velocity  $U_0$  is imposed at the upstream inlet, and a constant pressure  $p_d$  is specified at the downstream outlet. The grid size for the fluid and the channel wall is  $dx = 0.01D$  and  $ds = 0.005D$ , respectively. The fluid flow through a 2-D asymmetric stenosis at  $Re = 200$  is simulated and is validated against the commercial software ANSYS Fluent.

Figure 4 shows the simulated pressure, streamwise velocity and vorticity contours at  $tU_0/D = 100$  (the flow reaches a steady state) for 1 iteration and 5 iterations, respectively. As shown in the pressure contours, a low-pressure area is observed at the posterior part of the stenosis. Compared with the pressure

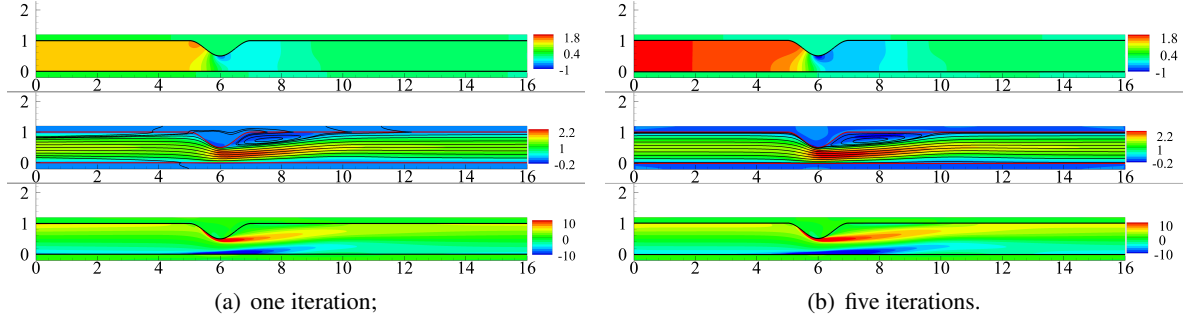


**Figure 4:** Pressure, streamwise velocity, and vorticity contours of a 2-D asymmetric stenosis at  $tU_0/D = 100$  for 1 iteration and 5 iterations, respectively. The velocity is non-dimensionalized by inlet averaged velocity  $U_0$ . The pressure here is relative pressure to the outlet pressure  $p_d$  and is non-dimensionalized by  $\rho U_0^2$ .

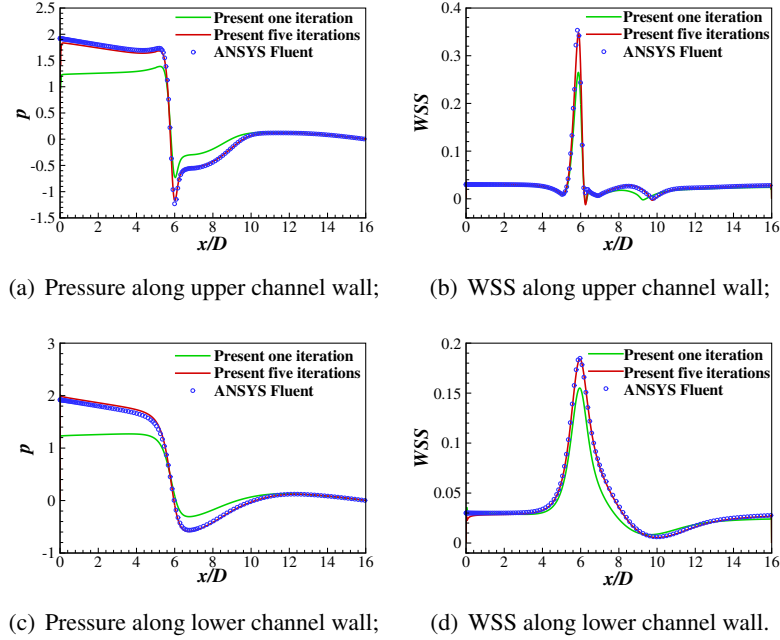


**Figure 5:** Pressure and wall shear stress (WSS) along the upper and lower channel walls at  $tU_0/D = 100$ . The pressure here is relative pressure to the outlet pressure  $p_d$ . The pressure and WSS are non-dimensionalized by  $\rho U_0^2$ .

contours for 1 iteration, a much higher pressure region is observed in the upstream channel of the stenosis for 5 iterations. The velocity contours show that a stable jet flow is formed downstream of the stenosis. The jet flow is stronger for the 5 iterations. The streamlines penetrate through the upper and lower channel walls in the velocity contours for 1 iteration, but not for 5 iterations. These observations demonstrate that the iterative IBM can suppress the spurious flow penetration and improve the no-penetration boundary conditions at the walls. The vorticity contours show that there is no vortex shedding downstream of the stenosis. The vortices are stretched further downstream of the stenosis for the five iterations.

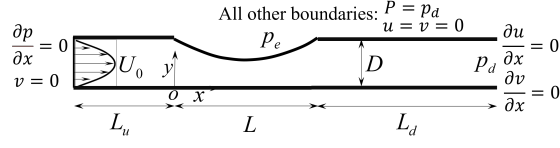


**Figure 6:** Schematic diagram of one-sided collapsible channel flow. All other boundaries: all other computational boundaries except for the inlet and outlet.

The pressure and wall shear stress (WSS) on the arterial wall are of great interest to the medical community as they play an essential role in the genesis and progression of cardiovascular diseases [15]. Therefore, the distributions of pressure and WSS along the upper and lower channel walls are shown in figure 5. The pressure and WSS are linearly interpolated based on the corresponding values at 2.5 and 5.0 grid points inward of the channel walls [3, 4]. Results of one iteration largely under-predict the pressure and WSS because the no-slip and no-penetration boundary conditions at the channel walls are not exactly satisfied. This issue can be well addressed by 5 iterations of the IBM, which allows for local flow reconstruction in the vicinity of the channel walls [4] and the results agree very well with those of ANSYS. Thus, the iteration improves the enforcement of the no-slip and no-penetration boundary conditions on the channel walls.

### 3.4 One-sided collapsible channel flow

Here, the iteration effects of the IBM are examined for an internal flow with a moving and deformable boundary by considering a 2-D incompressible flow in a one-sided collapsible channel. As shown in figure 6, a part of the channel wall is replaced by an elastic beam. The elastic beam has length  $L$  and is subjected to an external pressure  $p_e$ . The rigid channel has a width of  $D$ . A steady Poiseuille flow with averaged velocity  $U_0$  is imposed at the upstream inlet, and a constant pressure  $p_d$  is specified at the downstream outlet. The averaged flow velocity at the inlet  $U_0$ , channel height  $D$ , and fluid density  $\rho$  are used to non-dimensionalize this system, giving five non-dimensional parameters: the Reynolds number, the structure-to-fluid mass ratio, the stretching stiffness, the bending stiffness and the external pressure, which are respectively given by

$$Re = \frac{U_0 D}{\nu}, M = \frac{\rho_s}{\rho D}, K_s = \frac{Eh}{\rho U_0^2 D}, K_b = \frac{EI}{\rho U_0^2 D^3}, P_e = \frac{p_e - p_d}{\rho U_0^2}. \quad (6)$$

Here  $Re = 250$ ,  $M = 1.0$ ,  $K_s = 56.88$  and  $P_e = 1.95$  are used. A no-slip boundary condition is applied along the channel wall, including the elastic segment. Clamped conditions are used at the two ends of the elastic wall. The remaining parameters are  $L_u = 5D$ ,  $L_d = 30D$ ,  $L = 5D$ , and  $K_b/K_s = (h^2/12D^2) \approx 10^{-5}$  for a wall thickness  $h$  of 1% of the channel height. The nonlinear dynamics of the collapsible channel wall is treated as a Bernoulli-Euler beam with zero initial tension and solved by the finite difference method. The grid size for the fluid and the channel walls is  $0.01D$  and  $0.005D$ , respectively. More computational details can be found in our previous work [3, 4]. Here the iteration effects of the IBM are examined by considering four cases: 1 iteration, 3 iterations, 5 iterations and dynamic iterations. For the dynamic iterations, the iteration is terminated when the maximum velocity error at the immersed boundary is less than a pre-set criterion (i.e.  $\max(U_{error}(s, t)) \leq 5 \times 10^{-3}$ ) [4],

$$U_{error}(s, t) = \frac{\sqrt{(\mathbf{U}_{ib}^m(s, t) - \mathbf{U}(s, t))^2}}{U_0}. \quad (7)$$

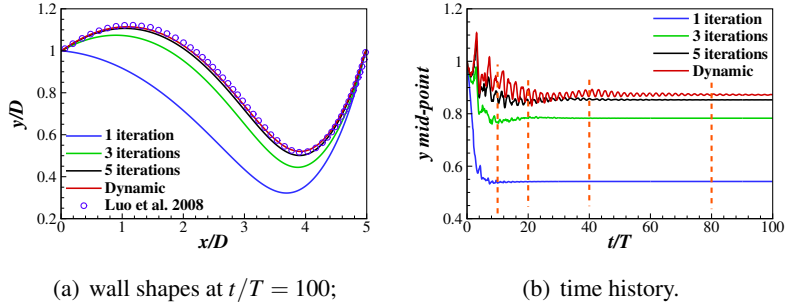


**Figure 7:** (a) comparison of wall shapes from present IB-LBM with the ALE (arbitrary Lagrangian Eulerian) of Luo et al. [16]; (b) the time history of the  $y$ -coordinate for the mid-point ( $x = 2.5$  initially) on the upper elastic wall for different iteration strategies: 1 iteration, 3 iterations, 5 iterations and dynamic iterations.  $T = D/U_0$  is the reference time.

**Table 2:** Averaged-flux error over the monitored locations.

Sources	Averaged-flux error
1 iteration	39.06%
3 iterations	11.52%
5 iterations	3.68%
Dynamic	1.33%

Figure 7(a) shows the comparison of wall shapes from present simulations with the ALE of Luo et al. [16]. The simulation with dynamic iterations predicts the most accurate wall shape while the 1 iteration predicts the worst. Figure 7(b) shows the time history of the  $y$ -coordinate of the mid-point of the upper elastic wall for different iterations. It shows that the time histories of the  $y$ -coordinate are quite different not only in the final value but also in the oscillation trajectory. For the dynamic iterations, the oscillations are evident during the transition state ( $0 \leq t/T \leq 50$ ) while the oscillation amplitude is gradually damped out as time increases.

In order to examine the boundary velocity slip error, the velocity error along the elastic wall, as shown in figure 8, is calculated at  $t/T = 10$ ,  $t/T = 20$ ,  $t/T = 40$ , and  $t/T = 80$ , respectively. It shows that the maximum velocity error is on the collapsible part of the wall ( $x/D \approx 1.4$ ) at all four instants. Serious boundary velocity slip error is on the channel wall from the inlet to the end of the elastic wall, and this error can be significantly (more than an order of magnitude) reduced by five iterations. For the dynamic iterations, the overall velocity error is the smallest among all the four iteration strategies.

The effects of the inlet velocity is tested by varying  $U_0 = 0.1$ ,  $0.05$ , and  $0.025$ . Figure 9(a) shows that the wall shape is approaching the correct value of Luo et al. [16] as the decrease of  $U_0$ . This is because the velocity error decreases as the decrease of the inlet velocity (i.e., reference velocity  $U_0$ ). Flow flux distributions at different monitored locations along the channel are traced and shown in figure 9(b). The averaged-flux error over the monitored locations are shown in table 2. For 1 iteration, there is a sharp decrease of flux from  $x/D = -5$  to  $x/D = 5$ , suggesting there is a significant flow penetration in this channel section. While the flux reduction is slow after  $x/D = 5$ . The flux reduction is significantly

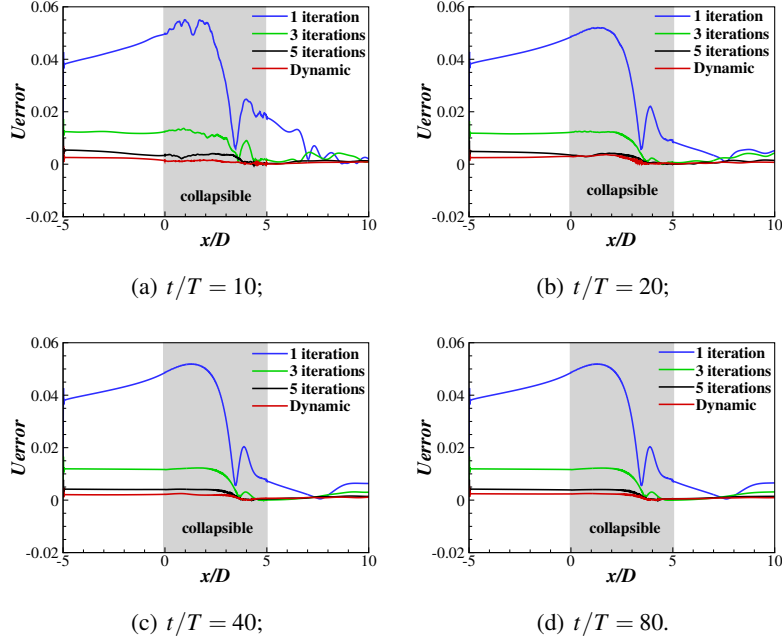


**Figure 8:** Velocity error  $U_{error}$  distributions on the upper channel wall (only for  $-5 \leq x/D \leq 10$ ) at four different instants:  $t/T = 10$ ,  $t/T = 20$ ,  $t/T = 40$ , and  $t/T = 80$  as indicated by dash lines in figure 7(b). The collapsible segment of the upper channel wall is highlighted by a grey shaded area.

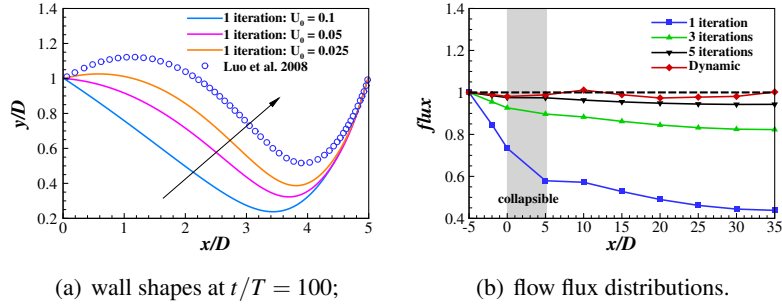


**Figure 9:** (a) wall shapes for 1 iteration under different inlet velocities  $U_0$ ; (b) Flow flux distributions at monitored cross sections along the channel at  $t/T = 100$ . All fluxes are normalized by the flux at the inlet ( $x/D = -5$ ) of the channel. The monitored locations are  $x/D = -5, -2, 0, 5, 10, 15, 20, 25, 30, 35$ .

improved from 1 iteration to 3 iterations with the averaged-flux error decrease from 39.06% to 11.52%. The averaged-flux error is further improved within 5% (i.e., 3.68%) after 5 iterations.

Figure 10 shows the time history of the iteration number  $m$  for the dynamic iterations. For the feedback coefficient  $\beta = 2m/s$  (the unit of the feedback coefficient can be found in the dimensional analysis in Appendix A), the iteration number fluctuates during the transition stage  $0 \leq t/T \leq 40$  and is constant after  $t/T = 42$ . The average iteration number is 6.17, causing an increase in the computational cost. In order to decrease the computational cost, a correction of the feedback coefficient  $\beta = 5.2m/s$  is derived (the derivation can be found in Appendix B). Here the correction coefficient is determined by the 4-point

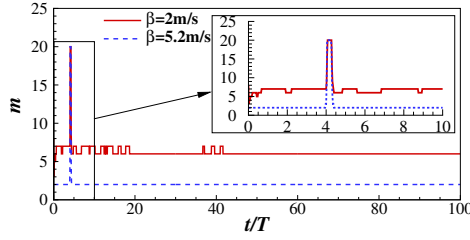


**Figure 10:** Time history of the iteration number  $m$  of the dynamic iterations. The iteration number decreases when the corrected feedback coefficient  $\beta = 5.2m/s$  used.

discrete delta function and the method of how the velocity is updated. For  $\beta = 5.2m/s$ , the iteration number is 2 everywhere except at  $t/T \approx 4$  when it is 20. The jump of the iteration number at  $t/T \approx 4$  is due to the elastic wall undergoing a sharp collapse, as shown in figure 7(b). The averaged iteration number decreases from 6.17 to 2.05.

#### 4 CONCLUSIONS

The performance of three implementations of the feedback IBM has been studied. The streamline penetration, velocity error on the immersed boundary and consequences in the force production and structure deformation are discussed by simulating external (a uniform flow over a flapping foil, flow-induced vibration of a flexible beam attached behind a cylinder) and internal flows (flow through a 2-D asymmetric stenosis and collapsible channel). Results show that the widely reported streamline penetration can be significantly reduced by the iterative IBM. The boundary velocity error does significantly affect the force production and structure deformation for external flows. However, for internal flows such as the stenosis and the collapsible channel flows, reducing the velocity error by using the iterative IBM substantially improves the prediction of the force distribution and structure deformation. Moreover, the value of the feedback coefficients could be smaller for the iterative IBM, which is very attractive for improving numerical stability for low structure-to-fluid mass ratio cases but at the expense of more iterations.

#### 5 ACKNOWLEDGEMENT

Dr F.-B. Tian is the recipient of an Australian Research Council Discovery Early Career Researcher Award (project number DE160101098). This work was also supported by Asian Office of Aerospace Research and Development (grant nos. FA2386-19-1-4066 and FA2386-20-1-4084) and Office of Naval Research Global (grant nos. N62909-20-1-2088). The computation work of this research was performed on the National Computational Infrastructure (NCI) supported by the Australian Government.

#### A APPENDIX: DIMENSIONAL ANALYSIS

Three basic dimensions: density  $\rho$ , time  $T$  and length  $L$  are chosen here. We denote the dimension of a variable  $q$  by  $[q]$ . For example, the dimension of the velocity  $[\mathbf{U}] = LT^{-1}$ . Consider Newton's second law, generically stated as  $[force] = [mass] \times [acceleration]$ . The dimension of the  $[force]$  can be expressed based on the three basic dimensions,

$$[force] = N \equiv [mass] \times [acceleration] = \rho L^3 \times LT^{-2} = \rho L^4 T^{-2}. \quad (8)$$

Then, the dimension of the force is  $[force] = \rho L^4 T^{-2}$ . For 3-D scenarios, the unit of the Lagrangian force density  $\mathbf{F}_{ib}$  is  $N/m^2$ . Then, the dimension of the Lagrangian force density is

$$[\mathbf{F}_{ib}] = N/m^2 = \rho L^4 T^{-2} / L^2 = \rho L^2 T^{-2}. \quad (9)$$

In the immersed boundary method,  $\mathbf{F}_{ib} = \beta \rho \Delta \mathbf{U}$ , this gives

$$[\mathbf{F}_{ib}] = [\beta \rho \Delta \mathbf{U}] = [\beta] \rho L T^{-1}. \quad (10)$$

Then, the dimension of the feedback coefficient  $[\beta] = L T^{-1} = m/s$ . For 2-D scenarios, the unit of the Lagrangian force density  $\mathbf{F}_{ib}$  is  $N/m$ . The unit of the mass  $[M] = \rho L^2$ . Substitute these two units into the above equations, one can get the same dimension of the feedback coefficient  $\beta$ .

## B APPENDIX: DERIVATION OF THE FEEDBACK COEFFICIENT

For simplicity, only the 2-D case is presented; the extension to 3-D is straightforward.

$$\mathbf{F}_{ib}(s, t) = \beta \rho(\mathbf{x}, t)(\mathbf{U}(s, t) - \mathbf{U}_{ib}(s, t)) = \beta \rho \Delta \mathbf{U}, \quad (11)$$

where  $\Delta \mathbf{U} = \mathbf{U} - \mathbf{U}_{ib}$ . Then, the body force density  $\mathbf{f}(\mathbf{x}, t)$  can be rewritten as

$$\mathbf{f}(\mathbf{x}, t) = \int \mathbf{F}_{ib}(s, t) \delta(\mathbf{x} - \mathbf{X}(s, t)) ds \approx \sum \beta \rho \Delta \mathbf{U} \delta(\mathbf{x} - \mathbf{X}) ds, \quad (12)$$

where  $ds$  is the discrete arc length of the immersed boundary.

$$\mathbf{U}_{ib} = \int \mathbf{u} \delta(\mathbf{x} - \mathbf{X}) dx \approx \sum \mathbf{u} \delta(\mathbf{x} - \mathbf{X}) \Delta V_x, \quad (13)$$

where  $\Delta V_x = \Delta x \Delta y$  is the local lattice volume. Then  $\Delta \mathbf{U}$  can be rewritten as

$$\Delta \mathbf{U} = \mathbf{U} - \sum \mathbf{u} \delta(\mathbf{x} - \mathbf{X}) \Delta V_x. \quad (14)$$

Then, the Lagrangian surface force density  $\mathbf{F}_{ib}(s, t)$  can be approximated as

$$\mathbf{F}_{ib} \approx \beta \rho [\mathbf{U} - \sum \mathbf{u} \delta(\mathbf{x} - \mathbf{X}) \Delta V_x]. \quad (15)$$

After performing the IBM, the fluid velocity near to the immersed boundary is updated by

$$\mathbf{u} = \mathbf{u} + \frac{\mathbf{f} \Delta t}{2\rho}. \quad (16)$$

If the no-slip and no-penetration boundary conditions are exactly satisfied at the solid boundary, then

$$0 = \Delta \mathbf{U} = \mathbf{U} - \sum (\mathbf{u} + \frac{\mathbf{f} \Delta t}{2\rho}) \delta(\mathbf{x} - \mathbf{X}) \Delta V_x. \quad (17)$$

From equation 14, one can get

$$\mathbf{U} = \Delta \mathbf{U} + \sum \mathbf{u} \delta(\mathbf{x} - \mathbf{X}) \Delta V_x. \quad (18)$$

Substituting equation 18 into equation 17, this gives

$$\begin{aligned}
 0 &= \Delta U + \sum \mathbf{u} \delta(\mathbf{x} - \mathbf{X}) \Delta V_x - \sum \left( \mathbf{u} + \frac{\mathbf{f} \Delta t}{2\rho} \right) \delta(\mathbf{x} - \mathbf{X}) \Delta V_x \\
 &= \Delta U + \sum \mathbf{u} \delta(\mathbf{x} - \mathbf{X}) \Delta V_x - \sum \mathbf{u} \delta(\mathbf{x} - \mathbf{X}) \Delta V_x - \sum \frac{\mathbf{f} \Delta t}{2\rho} \delta(\mathbf{x} - \mathbf{X}) \Delta V_x \\
 &= \Delta U - \sum \frac{\mathbf{f} \Delta t}{2\rho} \delta(\mathbf{x} - \mathbf{X}) \Delta V_x.
 \end{aligned} \tag{19}$$

Substituting equation 12 into equation 19, this gives

$$\begin{aligned}
 0 &= \Delta U - \sum \frac{\mathbf{f} \Delta t}{2\rho} \delta(\mathbf{x} - \mathbf{X}) \Delta V_x \\
 &= \Delta U - \Delta U \frac{\beta ds \Delta t \Delta V_x}{2} \sum [\sum \delta(\mathbf{x} - \mathbf{X})] \delta(\mathbf{x} - \mathbf{X}) \\
 &= \Delta U \left\{ 1 - \frac{\beta ds \Delta t \Delta V_x}{2} \sum [\sum \delta(\mathbf{x} - \mathbf{X})] \delta(\mathbf{x} - \mathbf{X}) \right\}.
 \end{aligned} \tag{20}$$

Then, this gives

$$\beta = \frac{2}{ds \Delta t \Delta V_x \sum [\sum \delta(\mathbf{x} - \mathbf{X})] \delta(\mathbf{x} - \mathbf{X})}. \tag{21}$$

The 4-point discrete delta function  $\delta(\mathbf{x} - \mathbf{X})$  is approximated by the Dirac delta function,

$$\delta(\mathbf{x} - \mathbf{X}) = \frac{1}{\Delta x \Delta y} \phi\left(\frac{x-X}{\Delta x}\right) \phi\left(\frac{y-Y}{\Delta y}\right). \tag{22}$$

Then, the feedback coefficient  $\beta$  can be approximated by

$$\begin{aligned}
 \beta &= \frac{2\Delta x \Delta y \Delta x \Delta y}{ds \Delta t \Delta x \Delta y \sum \left[ \sum \phi\left(\frac{x-X}{\Delta x}\right) \phi\left(\frac{y-Y}{\Delta y}\right) \right] \phi\left(\frac{x-X}{\Delta x}\right) \phi\left(\frac{y-Y}{\Delta y}\right)} \\
 &= \frac{2\Delta x \Delta y}{ds \Delta t \sum \left[ \sum \phi\left(\frac{x-X}{\Delta x}\right) \phi\left(\frac{y-Y}{\Delta y}\right) \right] \phi\left(\frac{x-X}{\Delta x}\right) \phi\left(\frac{y-Y}{\Delta y}\right)}.
 \end{aligned} \tag{23}$$

If the solid grid spacing  $ds = 0.5\Delta x$ , this gives,

$$\begin{aligned}
 \beta &= \frac{4\Delta y}{\Delta t \sum \left[ \sum \phi\left(\frac{x-X}{\Delta x}\right) \phi\left(\frac{y-Y}{\Delta y}\right) \right] \phi\left(\frac{x-X}{\Delta x}\right) \phi\left(\frac{y-Y}{\Delta y}\right)} \\
 &= \beta^* \frac{\Delta y}{\Delta t} \approx 5.2,
 \end{aligned} \tag{24}$$

where  $\beta^* = 4 / (\sum \left[ \sum \phi\left(\frac{x-X}{\Delta x}\right) \phi\left(\frac{y-Y}{\Delta y}\right) \right] \phi\left(\frac{x-X}{\Delta x}\right) \phi\left(\frac{y-Y}{\Delta y}\right))$  is a non-dimensional value. The dimension of  $\Delta x / \Delta t$  is  $[\Delta x / \Delta t] = m/s$ , which again confirms the dimension of the feedback coefficient  $[\beta] = m/s$ .

## REFERENCES

- [1] Huang WX, Tian FB. Recent trends and progress in the immersed boundary method. *Proc. Inst. Mech. Eng. C: J. Mech. Eng. Sci.* (2019) 233(23-24):7617-36.
- [2] Feng ZG, Michaelides EE. The immersed boundary-lattice Boltzmann method for solving fluid–particles interaction problems. *J. Comput. Phys.* (2004) 195(2):602-28.
- [3] Huang, Q., Tian, F.B., Young, J., Lai, J.C.S. A diffused interface immersed boundary–lattice Boltzmann method for simulation of channel flow. *in: 22nd AFMC.* (2020).
- [4] Huang, Q., Tian, F.B., Young, J., Lai, J.C.S.. Transition to chaos in a two-sided collapsible channel flow. *J. Fluid Mech.* (2021) 926, A15.
- [5] Huang, Q., Wang, L., Tian, F.B., Young, J., Lai, J.C.S., A diffused interface immersed boundary–lattice Boltzmann method for simulation of stenosis. *in: 14th WCCM & ECCOMAS Congress.* (2021).
- [6] Huang, Q., Wang, L., Ravi, S., Tian, F.B., Young, J., Lai, J.C.S. Benchmarking a coupled finite element–immersed boundary–lattice Boltzmann method solver for simulations of collapsible tube flows, *in: ACCM2021,* (2021) p. 15.
- [7] Huang, Q., Mazharmanesh, S., Tian, F., Young, J., Lai, J.C.S., Ravi, S. CFD solver validations for simulating passively pitching tandem wings in hovering flight, *in: MODSIM2021.* (2021).
- [8] Zhu, Y., Tian, F.B., Young, J., Liao, J.C., Lai, J.C.S. A numerical study of fish adaption behaviors in complex environments with a deep reinforcement learning and immersed boundary–lattice Boltzmann method. *Sci. Rep.* (2021) 11, 1–20.
- [9] Kang, S.K., Hassan, Y.A. A comparative study of direct-forcing immersed boundary-lattice Boltzmann methods for stationary complex boundaries. *Int. J. Numer. Meth. Fluids* (2011) 66, 1132–1158.
- [10] Tao, S., He, Q., Chen, J., Chen, B., Yang, G., Wu, Z. A non-iterative immersed boundary-lattice Boltzmann method with boundary condition enforced for fluid–solid flows. *Appl. Math. Model.* (2019) 76, 362–379.
- [11] Gsell, S., Favier, J. Direct-forcing immersed-boundary method: A simple correction preventing boundary slip error. *J. Comput. Phys.* (2021) 435, 110265.
- [12] Huang, Q. Low Reynolds number turbulent FSI and its applications in biological flows. *Ph.D. thesis. The University of New South Wales.* (2021).
- [13] Johnson, A. A., and Tayfun E. T. Mesh update strategies in parallel finite element computations of flow problems with moving boundaries and interfaces. *Comput. Methods Appl. Mech. Eng.* 119.1-2 (1994): 73-94.
- [14] Tian FB, Dai H, Luo H, Doyle JF, Rousseau B. Fluid–structure interaction involving large deformations: 3D simulations and applications to biological systems. *J. Comput. Phys.* 258 (2014):451-69.
- [15] Huang, Q., Sun, J., Xu, C. Effects of waveform shape of pulsatile blood flow on hemodynamics in an artery bifurcation model. *Proc. Inst. Mech. Eng. C: J. Mech. Eng. Sci.* (2020) 235, 428–440.
- [16] Luo, X., Cai, Z., Li, W., Pedley, T. The cascade structure of linear instability in collapsible channel flows. *J. Fluid Mech.* (2008) 600, 45–76.